RESEARCH ARTICLE

Chiral chromatography and surface chirality of carbon nanoparticles

Misché A. Hubbard[1,2,3] | **Chloe Luyet**[1] | **Prashant Kumar**[1,2] |
Paolo Elvati[4] | **J. Scott VanEpps**[2,3,5,6,7] | **Angela Violi**[1,4,9,10] |
Nicholas A. Kotov[1,2,5,6,8]

[1]Department of Chemical Engineering, University of Michigan, Ann Arbor, Michigan, USA

[2]Biointerfaces Institute, University of Michigan, Ann Arbor, Michigan, USA

[3]Department of Emergency Medicine, University of Michigan, Ann Arbor, Michigan, USA

[4]Department of Mechanical Engineering, University of Michigan, Ann Arbor, Michigan, USA

[5]Department of Biomedical Engineering, University of Michigan, Ann Arbor, Michigan, USA

[6]Department of Macromolecular Science and Engineering, University of Michigan, Ann Arbor, Michigan, USA

[7]The Max Harry Weil Institute for Critical Care Research and Innovation, University of Michigan, Ann Arbor, Michigan, USA

[8]Department of Materials Science and Engineering, University of Michigan, Ann Arbor, Michigan, USA

[9]Biophysics Program, University of Michigan, Ann Arbor, Michigan, USA

[10]Department of Electrical Engineering and Computer Science, University of Michigan, Ann Arbor, Michigan, USA

Correspondence
Nicholas A. Kotov, Department of Chemical Engineering, Biointerfaces Institute, University of Michigan, Ann Arbor, MI 48109, USA.
Email: kotov@umich.edu

J. Scott VanEpps, Department of Emergency Medicine, University of Michigan, Ann Arbor, MI 48109, USA.
Email: jvane@umich.edu

Angela Violi, Department of Mechanical Engineering, University of Michigan, Ann Arbor, MI 48109, USA.
Email: avioli@umich.edu

Abstract

Chiral carbon nanoparticles (CNPs) represent a rapidly evolving area of research for optical and biomedical technologies. Similar to small molecules, applications of CNPs as well as fundamental relationships between their optical activity and structural asymmetry would greatly benefit from their enantioselective separations by chromatography. However, this technique remains in its infancy for chiral carbon and other nanoparticles. The possibility of effective separations using high performance liquid chromatography (HPLC) with chiral stationary phases remains an open question whose answer can also shed light on the components of multiscale chirality of the nanoparticles. Herein, we report a detailed methodology of HPLC for successful separation of chiral CNPs and establish a path for its future optimization. A mobile phase of water/acetonitrile was able to achieve chiral separation of CNPs derived from *L*- and *D*-cysteine denoted as *L*-CNPs and *D*-CNPs. Molecular dynamics simulations show that the teicoplanin-based stationary phase has a higher affinity for *L*-CNPs than for *D*-CNPs, in agreement with experiments. The experimental and computational findings jointly indicate that chiral centers of chiral CNPs are

[This article is part of the Special Issue: Chirality Materials.]

present at their surface, which is essential for the multiple applications of these chiral nanostructures and equally essential for interactions with biomolecules and circularly polarized photons.

1 | INTRODUCTION

Carbon nanoparticles (CNPs) have attracted extensive research interest for their unique physicochemical properties.[1–3] CNPs with an average diameter of <10 nm share the desirable optical and electronic properties of typical semiconductor nanoparticles while avoiding disadvantages such as intrinsic toxicity from the use of heavy metals, harsh synthesis conditions, and expensive starting materials.[4–6] CNPs and other nanocarbons display strong photoluminescence, easy functionalization, exceptional biocompatibility, high stability, and chemical inertness, making them useful for an array of applications including light emitting diodes,[7] biosensors,[8] photocatalysts,[9] bioimaging,[10] and drug delivery.[11]

Mirror asymmetric CNPs with multiple scales of chirality from molecular to nanoscale have the advantages of achiral CNPs with the added capability of chiral recognition for biochemical, biomedical, and sustainability applications involving biomolecues with similar hierarchy of chirality. One can expect that multiscale enantiomers of CNPs would elicit distinctly different, biological and pharmacological responses. For example, L-CNPs made from *L*-lysine remodeled the secondary structure of amyloid-β (aβ-42) peptides and inhibited key factors of pathogenesis, including cytolysis and amyloid fibril fibrillation, while D-CNPs made from *D*-lysine displayed little to no biological activity against the same peptide.[12] Here we will refer to L- and D-NPs, when they are made from L- or D enantiomer of a molecular precursor, respectively. These notations represent only the chemical pathway for synthesis rather than the actual handedness at some scale. In another example, cysteine-derived *L*-CNPs upregulated glycolysis within human bladder cancer T24 cells, while *D*-CNPs did not display similar effects.[13] Chiral CNPs synthesized from cysteine electrostatically interact with porphyrins to form supramolecular porphyrins–CNP hybrids, where the chirality of the CNPs transfers to the porphyrins and the CD signal are enhanced.[14] Apart from graphene quantum dots,[15] the localization of chiral centers and other chiral geometries within the CNPs remains an open question. CNPs were reported to have predominantly spherical geometries but could potentially have chiral geometries at multiple scales. Among those, CNPs are hypothesized to have the tetrahedral coordinated carbon centers inherited from chiral precursors but it is not clear whether these molecular structures can survive the high-temperature carbonization processes used for their preparation. Additionally, CNPs may also display nanoscale chirality associated both with ligand distribution at the interface and twist-distortions in the CNP interior.[16] All of these structural features will result in a chiral environment around chromophores that will generate optical activity.[17–19]

The potential use of chiral CNPs for applications in biology, medicine, catalysis, and optics motivates us to determine whether the chiral centers in CNPs are located in the interior or at the interface of the particles. Importantly, the same question emerges when one needs to find reproducible methods for separating enantiomeric NPs. High performance liquid chromatography (HPLC) is the gold-standard method for chiral separations but has not been extended to resolving chiral nanoparticle solutions. Solution gradients are widely used for HPLC to separate analytes with disparate chemical composition. Chiral separations are typically conducted in isocratic conditions, making the mobile phase essential for separation yet difficult to optimize.[20] Here, chiral resolution of cysteine-derived chiral CNPs was achieved using a simple water/acetonitrile mobile phase. To the best of our knowledge, this is the first report on enantioselective HPLC for the separation of enantiomeric NPs. The chiral stationary phase (CSP) employs the macrocyclic glycopeptide teicoplanin as the chiral selector grafted to silica gel via linkage chains and has been ideal for separating un-derivatized amino acids and other polar ionic chiral compounds.[21–23] Molecular dynamics simulations show that *D*-CNPs preferentially interact with teicoplanin compared to *L*-CNPs, which is in agreement with the longer retention time of *D*-CNPs found experimentally. Chiral HPLC analysis of chiral nanostructures can determine enantiomeric nanoparticle purity and provide new methods for chiral separation and isolation. Simultaneously, these findings indicate that the surface of CNPs contains chiral centers.

2 | EXPERIMENTAL SECTION

2.1 | Materials

CNP precursors, namely, *L*-cysteine (*L*-cys) or *D*-cysteine (*D*-cys) and sodium hydroxide (NaOH), were purchased from Millipore Sigma. Racemic mixture of the amino acid cysteine (*rac*-cys) was prepared by mixing equal volumes of solution of *L*-cys and *D*-cys with a concentration of 1 mg/ml. Dialysis tubes with molecular weight cut off 1 kDa was obtained from Fischer Scientific. Acetonitrile (HPLC grade) was purchased from Millipore Sigma. All solutions were prepared using ultrapure water (18.2 MΩ·cm).

2.2 | Synthesis of *L*- or *D*-CNPs

Chiral CNPs were synthesized asymmetrically by a hydrothermal method as previously described.[24] *L*-cys or *D*-cys at 0.5 g and NaOH at 1 g were dissolved in 10 ml of water under ultrasonification for 20 min. The prepared solution was transferred into a 25 ml Teflon lined autoclave and heated at 120°C for 16 h. The mixture was dialyzed to remove unreacted material for 3 days. The final product was filtered against a 0.22 μm filter to remove large aggregates and then lyophilized for storage. Optically pure *L*- and *D*-CNPs were re-suspended to a final concentration of 1 mg/ml in ultrapure water prior to HPLC analysis.

2.3 | Circular dichroism

CD spectra were acquired in a Jasco-815 spectrophotometer. The spectra were recorded from 190 to 500 nm, at 1 nm intervals, 1 nm bandwidth, and a scan speed of 100 nm/min.

2.4 | Vibrational circular dichroism

VCD measurements were performed on CNP dispersions in heavy water (D_2O) at a concentration of 33 mg/ml. A 100 μl drop was sandwiched between two BaF_2 crystals separated by 50 μm Teflon spacer. MCT-V detector was used to acquire IR and VCD data in the range 1,800–850 cm^{-1} with a resolution of 4 cm^{-1} and a total of 200 and 1,000 accumulations, respectively. The sandwiched dispersion between BaF_2 crystals was rotated along an axis coinciding with the direction of the beam at a constant speed to avoid settling of particles.

Corresponding IR and VCD were plotted as absorbance (A) and differential absorbance of left and right circularly polarized light (ΔA) respectively with exclusion of 1,300 to 1,100 cm^{-1} range that corresponds to strong absorption from D_2O.

2.5 | Chiral HPLC analysis

Chiral CNPs were separated using an Agilent 6000 Series LC/MS instrument with an Astec CHIROBIOTIC T 10 cm × 4.6 mm (Millipore Sigma) chiral column. The mobile phase consisted of ultrapure water and acetonitrile (30:70 v/v) applied over 10 min at a flow rate of 1 ml min^{-1}. UV detection was set to 205 nm.

2.6 | Molecular dynamics

The affinity of *L*- and *D*-CNPs with teicoplanin was computed with biased all-atom simulations. The CHARMM force field, version 36, was employed, and the systems were solvated using explicit TIP3P water.[25,26] First, systems were minimized and equilibrated in the isothermal-isobaric ensemble for at least 150 ns, where a Langevin piston Nose-Hoover method (with a period of 200 and 50 fs decay) maintained a pressure of 100 kPa. A Langevin thermostat (with a characteristic time of 20 ps) was used to keep the temperature constant. A time step of 2 fs was employed to integrate the equations of motion, and hydrogen atoms are kept rigid via the SHAKE algorithm. Non-bonded short-range interactions smoothly approached 0 using an X-PLOR switching function between 1 and 1.2 nm, in conjunction with the particle mesh Ewald algorithm to evaluate long-range Coulombic forces. Nanoscale Molecular Dynamics (NAMD) software was used for running the simulations.[27]

Free energy surfaces were reconstructed using well-tempered Metadynamics simulations in the canonical ensemble over the course of 630 ns or more.[28,29] Gaussian-shaped bias ($\sigma = 0.04$ nm, initial height 0.2 kcal/mol) was deposited with pace 0.4 ps, and scaled using a bias factor of 10. Simulations were biased on the distance between teicoplanin's center of mass (COM) and the COM of each chiral CNP (d_{COM}). A harmonic wall was placed at 5 nm. The free energy was calculated as the average probability difference between the bound state (distance $\leq$ 2.5 nm) and the unbound state (distance $\geq$ 3 nm). PLUMED 2 was used for all simulation.[30,31] Visual Molecular Dynamics (VMD) was used for data visualization, and the MDAnalysis and Matplotlib Python libraries were used for plottin and data analysis.[32–35]

3 | RESULTS AND DISCUSSION

Reversed-phase HPLC is the most common method for chiral analysis of amino acids and protein fragments. Analysis of protein fragments is achieved by chemical or enzymatic hydrolysis of proteins, followed by HPLC separation and, finally, analysis on mass spectrometry to identify protein sequence.[36] Chiral CNPs are similar in size (2–10 nm) and molecular weight (10^3–10^5 g/mol) to proteins, yet if their chiral moieties are located on the surface, hydrolysis will be unnecessary for chiral analysis.[37] Furthermore, biological molecules, namely, proteins, are known to adsorb onto the surface of CNPs changing the physicochemical properties of the NPs.[38] Chiral HPLC analysis can be employed to characterize protein coronas by analyzing changes in retention time, which suggests changes in polarity or chirality in the case of CNP induced racemization. This makes chiral HPLC analysis a powerful tool to understand enantiomeric interactions between biological molecules and chiral CNPs.

Chiral CNPs were synthesized using a hydrothermal route using cysteine as both the carbon and chiral precursor,[39] Figure 1A. Synthesis conditions (temperature and duration) were the same for synthesizing L-CNPs and D-CNPs to ensure their physicochemical properties were similar (size distribution, crystal structure, and surface functionalization). Subsequent characterization indicated that L-CNPs and D-CNPs have similar chemical structure and properties with exception of mirror symmetric relations between some chemical structures constituting the near-spherical particles. The main body of this manuscript will focus on the characterization of L-CNPs. More information on the physical and chemical properties of D-CNPs can be found in the supplemental information (SI).

Morphological characteristics of the chiral CNPs were obtained using transmission electron microscopy (TEM) images that reveal both L- and D-CNPs have a size distribution between 2–7 nm (Figure 1B), which may be expected to be a challenge in their characterization and separation by chromatography. Scanning transmission electron microscopy high-angle annular dark field images (STEM-HAADF) images in Figure 1C confirm the size distribution and morphology of NPs as seen in TEM images.

The electrokinetic zeta-potential (ζ) of chiral CNPs was measured to determine the sign and estimate the magnitude of the averasurface charge on the particles (Figure S1). At pH 7, chiral CNPs display a strong negative charge of -27 ± 0.66 mV and -28.7 ± 0.26 mV for L-CNPs and D-CNPs, respectively. The negative charge is
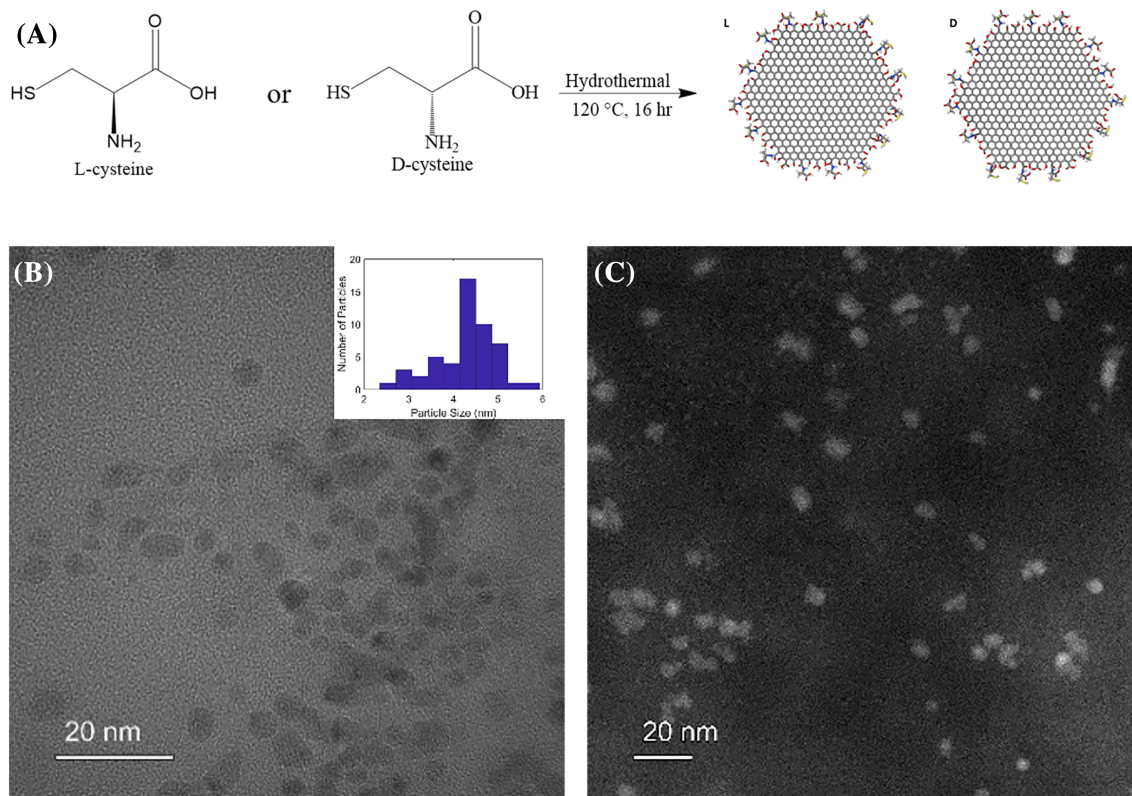
FIGURE 1 (A) Schematic of chiral CNP synthesis; the CNP cores are expected to contain both crystalline and noncrystalline areas (B) TEM of L-CNPs with histogram inlay; and (C) STEM image of L-CNPs

consistent with the presence of carboxyl groups at the edges.

The optical properties of chiral CNPs were observed using UV–vis spectroscopy. For both *L*- and *D*-CNPs, two peaks were seen at 200 and 280 nm, which are attributed to the π-π* transition of the sp^2 hybridized carbon network (Figure 2A).[15] Fourier Transform Infrared Spectroscopy (FT-IR) was employed to determine the functional groups conjugated to the surface of the chiral CNPs (Figure 2B). The broad absorption band between 3,200 and 3,600 cm^{-1} are attributed to –OH and –NH stretching vibrations. The peak at 2,970 cm^{-1} indicates C-H bonds. The vibrational signals near 1,750 and 1,620 cm^{-1} were attributed to C=O and C=C, respectively.[40] The presence of C-S bonds was seen by the absorption band at 1195 cm^{-1}. FT-IR spectra confirmed the presence of carboxyl, amino, and thiol groups at the surface of the chiral CNPs.

The photoluminescence spectra of chiral CNPs show the maximum emission wavelength between at ~475 nm after 365 nm excitation (Figure 2C,D). They indicate that the CNPs have typical light emission of conjugated aromatic compounds. The luminescence properties of these NPs are convenient for both analysis and biomedical applications.

Circular dichroism (CD) spectroscopy was used to investigate the chiroptical properties of the CNPs. CD spectra of *L*- and *D*- CNPs in Figure 3A reveal symmetrical and opposite high-energy peaks at 205 nm, which is the chiral signal from cysteine molecules. Both *L*- and *D*-CNPs gave rise to a new symmetrical CD signal at around 260 nm, which suggests there is an interaction between cysteine and the graphitic core of the CNPs.[41]

IR and vibrational circular dichroism (VCD) spectra were acquired to determine information about molcular scale chirality of CNPs. VCD data from previous reports of enantiomeric cysteine show mirror symmetry at the 1,621 cm^{-1} peak.[42] Indeed, the mirror symmetric opposite band at 1,600 cm^{-1} in Figure 3B indicates that the chirality is transferred from the cysteine molecules to the CNPs. The IR spectrum in Figure 3C shows an antisymmetric stretching vibration at 1,600 cm^{-1} of carboxyl
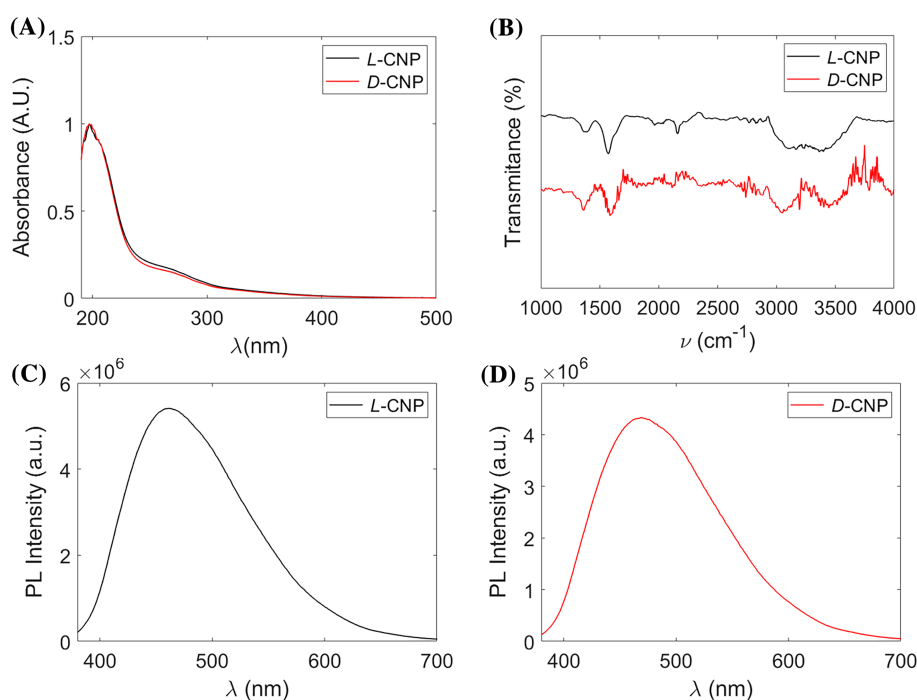
FIGURE 2 (A) UV–vis spectra of chiral CNPs; (B) FT-IR spectra of chiral CNPs; (C) PL spectrum of L-CNPs; and (D) PL spectrum of D-CNPs
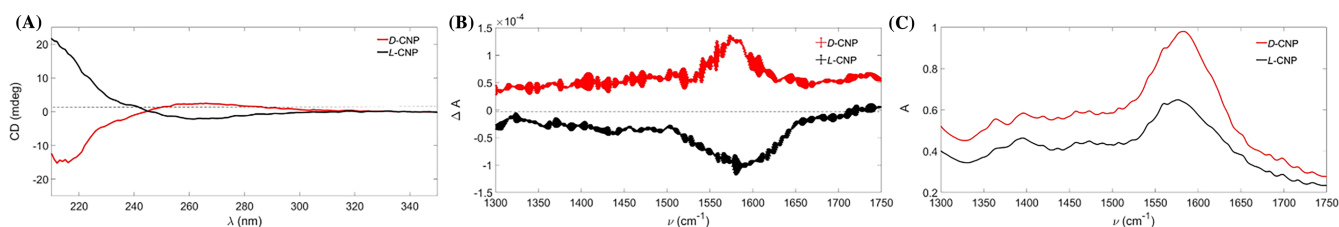
FIGURE 3 (A) CD spectra; (B) VCD spectra; and (C) IR spectra of chiral CNPs

groups, which agrees which FT-IR data found in Figure 2C. Owing to the organic nature of CNPs the VCD spectra is on the order of 10^{-4}.

The retention times of *rac*-cys and chiral CNPs can be found in Table 1. For *rac*-cys and chiral CNPs, the *D*-enantiomer had longer retention times compared to the *L*-enantiomer, which matches previous reports in literature.[23] *rac*-cys contained two retention times, where *L*-cys resolved at 3.305 ± 0.145 min and *D*-cys shortly after at 3.368 ± 0.017 min. Figure 4A shows the corresponding chromatogram for *rac*-cys separation. The chiral CNPs eluted much faster than their cysteine precursors at 0.795 ± 0.046 min and 0.961 ± 0.022 min for *L*-and *D*-CNPs, respectively (Figure 4B). The longer retention times of the CNPs indicates their size prevents them interacting with chiral bonding sites deep within the CSP. This suggests that chiral ligands at the surface of the

CNPs are the primary mechanism for enantioselective separation through polar ionic interactions.

The peak resolution may be improved by adding organic or alcohol modifiers to the mobile phase. Reducing the polarity of the solvent will lower the elution strength and allow more π-π interactions between the chiral CNPs and the CSP. The size distribution of the chiral CNPs may also allow individual particles to have non-uniform interactions along the column. Further purification and fractionation of the CNPs can lower the size distribution and may improve enantioselective separation.

Chiral CNPs were captured after separation to ensure they maintain their morphology and physicochemical properties. UV–vis spectroscopy found in Figure 5A shows two similar peaks at 200 and 260 nm as seen in Figure 2 indicating minimal changes to the crystal structure of the CNPs. This point is confirmed by emission spectra of eluted CNPs. After 365 nm excitation, the same high-energy peak can be found between 450–500 nm similar to that in Figure 2. TEM microscopy of eluted CNPs

TABLE 1 Retention times of rac-cys and chiral CNPs after separation on CHIROBIOTIC T column for HPLC

Analyte	Retention time 1 (min)	Retention time 2 (min)
rac-cys	3.305 ± 0.145	3.368 ± 0.017
L-CNP	0.795 ± 0.046	-
D-CNP	0.961 ± 0.022	-

TABLE 2 Binding free energy of teicoplanin and chiral CNPs

System	ΔA (kcal/mol)	Standard deviation
L-CNP	0.35	0.51
D-CNP	−1.95	0.64

FIGURE 4 Chromatograms of (A) rac-cys and (B) chiral CNPs separated on an Astec CHIROBIOTIC T column for HPLC
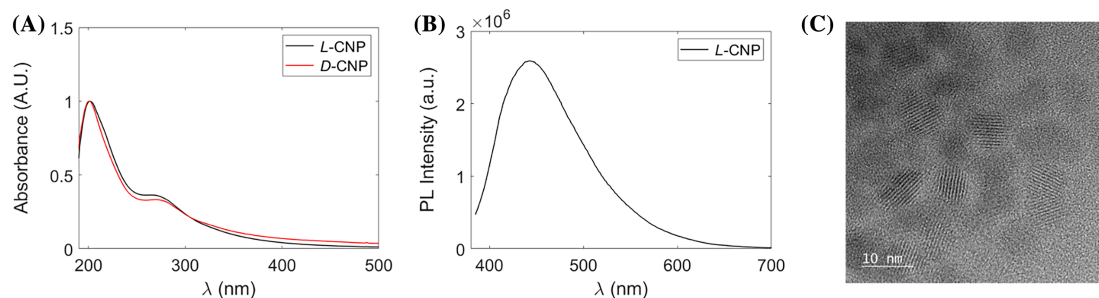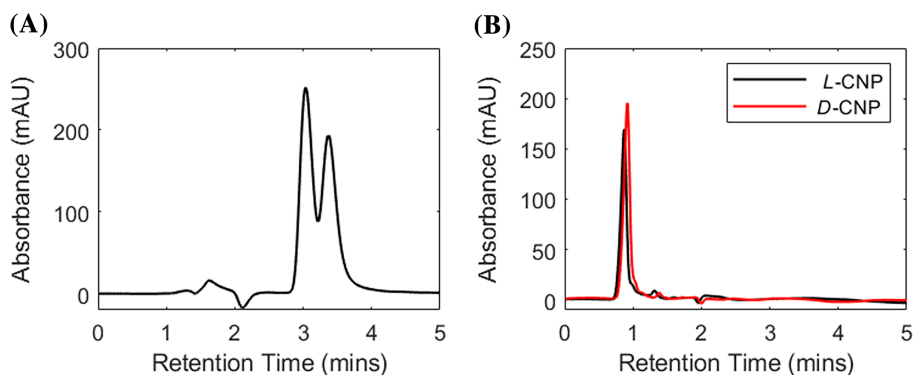
FIGURE 5 (A) UV–vis spectra; (B) emission spectrum; and (C) TEM image of L-CNPs following chiral separation
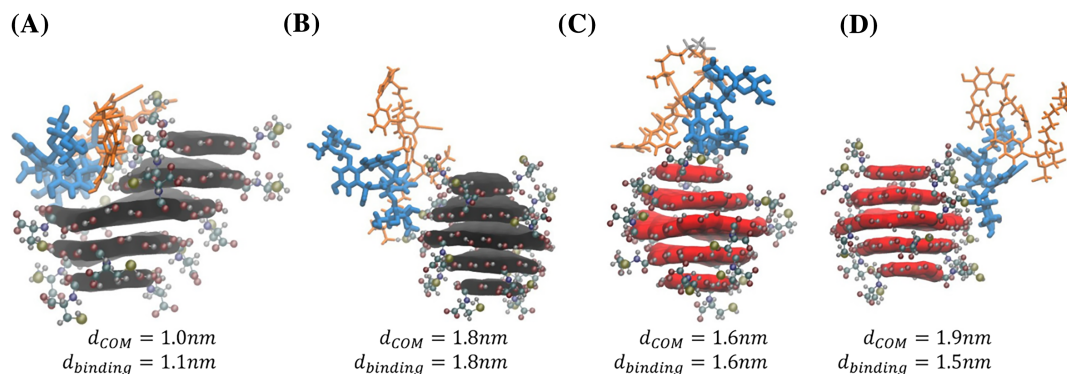
FIGURE 6 Chiral CNPs interacting with teicoplanin segments on the HPLC column. Teicoplanin (orange and blue), teicoplanin binding region (blue), D-CNP (red), and L-CNP (black)

maintain their size distribution of indicating the column separates by chirality and not by size. TEM also highlights the CNPs retain the lamellar structure of graphene, which proves CNPs are highly stable and resistant to hydrolysis. The stability of CNPs after separation allows the nanoparticles to be fractionated using HPLC for analysis or to be used in future experiments.

It has been established that teicoplanin is bound to aminopropyl silica gel through a bifunctional aliphatic isocyanate.[43] Nonetheless, an incomplete understanding of the covalent grafting makes in silico investigation more difficult.[44] Consequently, unbound teicoplanin was used to study its interaction with chiral CNPs using biased molecular dynamics (MD) simulations. Two simplified models were generated, one for teicoplanin with chiral NPs made from two cysteine enantiomers, under the mobile phase conditions stated above, to mimic the chromatographic conditions. Metadynamics simulations reveal a binding free energy for teicoplanin with L-and D-CNPs to be 0.35 ± 0.51 and -1.95 ± 0.64, respectively (Table 2), where the error is standard deviation. The higher binding energy for the teicoplanin/L-CNP system suggests a weaker or unfavorable interaction. Interestingly, L-CNPs become warped in close proximity to teicoplanin (Figure 6A); furthermore, the center of mass distance between teicoplanin's binding region and the L-CNP ($d_{binding}$) tends to be larger than for the D-CNP when they are interacting. For example, teicoplanin's binding region orients itself closer to the D-CNP in Figure 6D, a possible rationalization for the difference in affinity (Table 2). Overall, MD simulations highlight the higher binding affinity between teicoplanin and D-CNPs, confirming the elution order found in experiments. This suggests MD simulations can be powerful tools for understanding the interactions of chiral NPs and chiral selectors.[45,46] Furthermore, MD simulations can be employed to screen multiple parameters to find suitable conditions for enhanced resolution between enantiomers.

4 | CONCLUSIONS

Chiral CNPs made from two enantiomeric forms of cysteine were successfully separated using a water/acetonitrile mobile phase on an Astec CHIROBIOTIC T chiral column, which indicates the presence of chiral centers located on their surface. Besides the analytical importance enabling further development of biomedical and other applications of chiral nanoparticles, this finding is essential for the accurate physical picture of their interactions with cellular membranes[47] and biomacromolecules.[48] Various mirror asymmetric structures at multiple scales may also exist in the NP interior exemplified by the twist of their crystalline nanoparticle interior, helical conformation of molecular components, and a mirror-asymmetric surface. Unlike semiconductor and metal NPs,[49,50] the presence of these non-local components of multiscale chirality for CNPs remains uncertain. Furthermore, the condensation reactions leading to CNP formation are likely to lead to randomization and racemization of substituents around sp^3 carbons. The ability of HPLC columns with teicoplanin stationary phase to separate these L- and D-CNPs give strong indication that L- and D-centers of cysteine are retained. Additionally, these data indicate that chiral CNPs are hydrolytically stable and resist degradation into their precursor cysteine. The dominant forces behind chiral separations were steric hindrance and polar ionic. MD simulations were employed to investigate the interaction between chiral NPs and the chiral selector. This technique provides a new method for detecting and quantifying chiral NPs. While providing foundation for future chiral HPLC analysis of chiral NPs, chiral HPLC analysis of NPs can also provide an

analytical toolbox for future studies of chiral recognition mechanisms and methods for interacting with different chiral centers.

CONFLICT OF INTEREST

The authors declare they have no conflict of interest related to this work.

DATA AVAILABILITY STATEMENT

Data are available upon request from authors.

ORCID

Misché A. Hubbard https://orcid.org/0000-0003-3993-8226
Paolo Elvati https://orcid.org/0000-0002-6882-6023
Nicholas A. Kotov https://orcid.org/0000-0002-6864-5804

REFERENCES

1. Ragazzon G, Cadranel A, Ushakova EV, et al. Optical processes in carbon nanocolloids. *Chem.* 2021;7:606-628.
2. Kang Z, Lee ST. Carbon dots: advances in nanocarbon applications. *Nanoscale.* 2019;11(41):19214-19224. doi:10.1039/C9NR05647E
3. Rod KA, Smith AP, Leng W, et al. Water-dispersible nanocolloids and higher temperatures promote the release of carbon from riparian soil. *Vadose Zo J.* 2020;19(1):e20077. doi:10.1002/vzj2.20077
4. Chen F, Gao W, Qiu X, et al. Graphene quantum dots in biomedical applications: recent advances and future challenges. *Front Lab Med.* 2017;1(4):192-199. doi:10.1016/j.flm.2017.12.006
5. Zhang N, Zhang L, Ruan YF, Zhao WW, Xu JJ, Chen HY. Quantum-dots-based photoelectrochemical bioanalysis highlighted with recent examples. *Biosens Bioelectron.* 2017;94:207-218. doi:10.1016/j.bios.2017.03.011
6. Li L, Yan X. Colloidal graphene quantum dots. *J Phys Chem Lett.* 2010;1(17):2572-2576. doi:10.1021/jz100862f
7. Kumar GS, Thupakula U, Sarkar PK, Acharya S. Easy extraction of water-soluble graphene quantum dots for light emitting

8. diodes. *RSC Adv.* 2015;5(35):27711-27716. doi:10.1039/C5RA01399B
9. Wu X, Tian F, Wang W, Chen J, Wu M, Zhao JX. Fabrication of highly fluorescent graphene quantum dots using l-glutamic acid for in vitro/in vivo imaging and sensing. *J Mater Chem C.* 2013;1(31):4676-4684. doi:10.1039/c3tc30820k
10. Zeng Z, Chen S, Tan TTY, Xiao FX. Graphene quantum dots (GQDs) and its derivatives for multifarious photocatalysis and photoelectrocatalysis. *Catal Today.* 2018;315:171-183. doi:10.1016/j.cattod.2018.01.005
11. Chung S, Revia RA, Zhang M. Graphene quantum dots and their applications in bioimaging, biosensing, and therapy. *Adv Mater.* 2021;33(22):1904362. doi:10.1002/adma.201904362
12. Iannazzo D, Pistone A, Salamò M, et al. Graphene quantum dots for cancer targeted drug delivery. *Int J Pharm.* 2017;518(1-2):185-192. doi:10.1016/j.ijpharm.2016.12.060
13. Malishev R, Arad E, Bhunia SK, et al. Chiral modulation of amyloid beta fibrillation and cytotoxicity by enantiomeric carbon dots. *Chem Commun.* 2018;54(56):7762-7765. doi:10.1039/C8CC03235A
14. Li F, Li Y, Yang X, et al. Highly fluorescent chiral N-S-doped carbon dots from cysteine: affecting cellular energy metabolism. *Angew Chemie.* 2018;130(9):2401-2406. doi:10.1002/ange.201712453
15. Liu X, Lu J, Chen J, et al. Chiral self-assembly of porphyrins induced by chiral carbon dots. *Front Chem.* 2020;8:670. doi:10.3389/fchem.2020.00670
16. Suzuki N, Wang Y, Elvati P, et al. Chiral graphene quantum dots. *ACS Nano.* 2016;10(2):1744-1755. doi:10.1021/acsnano.5b06369
17. Visheratina A, Kumar P, Kotov N. Engineering of inorganic nanostructures with hierarchy of chiral geometries at multiple scales. *AIChE J.* 2022;68(1):e17438. doi:10.1002/aic.17438
18. Tedesco D, Bertucci C. Induced circular dichroism as a tool to investigate the binding of drugs to carrier proteins: classic approaches and new trends. *J Pharm Biomed Anal.* 2015;113:34-42. doi:10.1016/j.jpba.2015.02.024
19. Döring A, Ushakova E, Rogach AL. Chiral carbon dots: synthesis, optical properties, and emerging applications. *Light Sci Appl.* 2022;111(11):1-23.
20. Wei Y, Chen L, Wang J, Liu X, Yang Y, Yu S. Investigation on the chirality mechanism of chiral carbon quantum dots derived from tryptophan. *RSC Adv.* 2019;9(6):3208-3214. doi:10.1039/C8RA09649J
21. Pirok BWJ, Gargano AFG, Schoenmakers PJ. Optimizing separations in online comprehensive two-dimensional liquid chromatography. *J Sep Sci.* 2018;41(1):68-98. doi:10.1002/jssc.201700863
22. Aboul-Enein HY, Ali I. Chiral resolution of cromakalim by HPLC on teicoplanin and teicoplanin aglycon chiral stationary phases. *J Liq Chromatogr Relat Technol.* 2002;25(13-15):2337-2344. doi:10.1081/JLC-120014007
23. Berthod A. Chiral recognition mechanisms with macrocyclic glycopeptide selectors. *Chirality.* 2009;21(1):167-175. doi:10.1002/chir.20600
24. Claus JE. Chiral HPLC analysis of underivatized amino acid enantiomers. *Reporter.* 2011;29:8-9.
25. Hu L, Sun Y, Zhou Y, et al. Nitrogen and sulfur co-doped chiral carbon quantum dots with independent photoluminescence

and chirality. *Inorg Chem Front*. 2017;4(6):946-953. doi:10.1039/C7QI00118E

25. Huang J, Mackerell AD. CHARMM36 all-atom additive protein force field: validation based on comparison to NMR data. *J Comput Chem*. 2013;34(25):2135-2145. doi:10.1002/jcc.23354

26. Jorgensen WL, Chandrasekhar J, Madura JD, Impey RW, Klein ML. Comparison of simple potential functions for simulating liquid water. *J Chem Phys*. 1998;79:926.

27. Phillips JC, Braun R, Wang W, et al. Scalable molecular dynamics with NAMD. *J Comput Chem*. 2005;26(16):1781-1802. doi:10.1002/jcc.20289

28. Barducci A, Bonomi M, Parrinello M. Metadynamics. *Wiley Interdiscip Rev Comput Mol Sci*. 2011;1(5):826-843. doi:10.1002/wcms.31

29. Barducci A, Bussi G, Parrinello M. Well-tempered metadynamics: a smoothly converging and tunable free-energy method. *Phys Rev Lett*. 2008;100(2):020603. doi:10.1103/PhysRevLett.100.020603

30. Bonomi M, Branduardi D, Bussi G, et al. PLUMED: a portable plugin for free-energy calculations with molecular dynamics. *Comput Phys Commun*. 2009;180(10):1961-1972. doi:10.1016/j.cpc.2009.05.011

31. Tribello GA, Bonomi M, Branduardi D, Camilloni C, Bussi G. PLUMED 2: new feathers for an old bird. *Comput Phys Commun*. 2014;185(2):604-613. doi:10.1016/j.cpc.2013.09.018

32. Michaud-Agrawal N, Denning EJ, Woolf TB, Beckstein O. MDAnalysis: a toolkit for the analysis of molecular dynamics simulations. *J Comput Chem*. 2011;32(10):2319-2327. doi:10.1002/jcc.21787

33. Hunter JD. Matplotlib: a 2D graphics environment. *Comput Sci Eng*. 2007;9(3):90-95. doi:10.1109/MCSE.2007.55

34. Gowers R, Linke M, Barnoud J, et al. MDAnalysis: a python package for the rapid analysis of molecular dynamics simulations. *Proc 15th Python Sci Conf*. 2016;98–105.

35. Humphrey W, Dalke A, Schulten KVMD. Visual molecular dynamics. *J Mol Graph*. 1996;14(1):33-38. doi:10.1016/0263-7855(96)00018-5

36. Ali I, Suhail M, Aboul-Enein HY. Chiral analysis of macromolecules. *J Liq Chromatogr Relat Technol*. 2018;41(11):749-760. doi:10.1080/10826076.2018.1514509

37. Wang Y, Kadiyala U, Qu Z, et al. Anti-biofilm activity of graphene quantum dots via self-assembly with bacterial amyloid proteins. *ACS Nano*. 2019;13(4):4278-4289. doi:10.1021/acsnano.8b09403

38. Huang R, Carney RP, Stellacci F, Lau BLT. Protein–nanoparticle interactions: the effects of surface compositional and structural heterogeneity are scale dependent. *Nanoscale*. 2013;5(15):6928-6935. doi:10.1039/c3nr02117c

39. Zhang Y, He J. Facile synthesis of S, N co-doped carbon dots and investigation of their photoluminescence properties. *Phys Chem Chem Phys*. 2015;17(31):20154-20159. doi:10.1039/C5CP03498A

40. Chen C, Zhao D, Hu T, Sun J, Yang X. Highly fluorescent nitrogen and sulfur co-doped graphene quantum dots for an inner filter effect-based cyanide sensor. *Sens Actuators B*. 2017;241:779-788. doi:10.1016/j.snb.2016.11.010

41. Qu D, Zheng M, Du P, et al. Highly luminescent S, N co-doped graphene quantum dots with broad visible absorption bands for visible light photocatalysts. *Nanoscale*. 2013;5(24):12272-12277. doi:10.1039/c3nr04402e

42. Kamiński M, Kudelski A, Pecul M. Vibrational optical activity of cysteine in aqueous solution: a comparison of theoretical and experimental spectra. *J Phys Chem B*. 2012;116(16):4976-4990. doi:10.1021/jp300699e

43. D'acquarica I, Gasparrini F, Misiti D, et al. Direct chromatographic resolution of carnitine and O-acylcarnitine enantiomers on a teicoplanin-bonded chiral stationary phase. *J Chromatogr a*. 1999;857(1-2):145-155. doi:10.1016/S0021-9673(99)00773-6

44. Sardella R, Ianni F, Cossignani L, Aldini G, Carotti A. Binding modes identification through molecular dynamic simulations: a case study with carnosine enantiomers and the Teicoplanin A2-2-based chiral stationary phase. *J Sep Sci*. 2020;43(9-10):1728-1736. doi:10.1002/jssc.202000092

45. Elvati P, Baumeister E, Violi A. Graphene quantum dots: effect of size, composition and curvature on their assembly. *RSC Adv*. 2017;7(29):17704-17710. doi:10.1039/C7RA01029J

46. Elvati P, Violi A. Free energy calculation of permeant–membrane interactions using molecular dynamics simulations. *Methods Mol Biol*. 2012;926:189-202. doi:10.1007/978-1-62703-002-1_14

47. Ostadhossein F, Vulugundam G, Misra SK, Srivastava I, Pan D. Chirality inversion on the carbon dot surface via covalent surface conjugation of cyclic α-amino acid capping agents. *Bioconjug Chem*. 2018;29(11):3913-3922. doi:10.1021/acs.bioconjchem.8b00736

48. Li F, Li S, Guo X, et al. Chiral carbon dots mimicking topoisomerase I to mediate the topological rearrangement of supercoiled DNA enantioselectively. *Angew Chem Int Ed*. 2020;59(27):11087-11092. doi:10.1002/anie.202002904

49. Kumar J, Thomas AKG, Liz-Marzán LM. Nanoscale chirality in metal and semiconductor nanoparticles. *Chem Commun*. 2016;52(85):12555-12569. doi:10.1039/C6CC05613J

50. Xia Y, Zhou Y, Tang Z. Chiral inorganic nanoparticles: origin, optical properties and bioapplications. *Nanoscale*. 2011;3(4):1374-1382. doi:10.1039/c0nr00903b

SUPPORTING INFORMATION

Additional supporting information can be found online in the Supporting Information section at the end of this article.

How to cite this article: Hubbard MA, Luyet C, Kumar P, et al. Chiral chromatography and surface chirality of carbon nanoparticles. *Chirality*. 2022; 34(12):1494-1502. doi:10.1002/chir.23507